Earth and Planetary Science Letters 448 (2016) 115–121

Contents lists available at ScienceDirect

Earth and Planetary Science Letters

www.elsevier.com/locate/epsl

Earth rotation changes since −500 CE driven by ice mass variations

Carling Hay [a,b,*], Jerry X. Mitrovica [b], Eric Morrow [a], Robert E. Kopp [a,c], Peter Huybers [b], Richard B. Alley [d]

[a] Department of Earth and Planetary Sciences and Institute of Earth, Ocean, and Atmospheric Sciences, Rutgers University, Piscataway, NJ, 08854, USA
[b] Department of Earth and Planetary Sciences, Harvard University, 20 Oxford Street, Cambridge, MA, 02138, USA
[c] Rutgers Energy Institute, Rutgers University, New Brunswick, NJ, 08901, USA
[d] Department of Geosciences and Earth and Environmental Systems Institute, Pennsylvania State University, University Park, PA, 16802, USA

ARTICLE INFO

Article history:
Received 1 October 2015
Received in revised form 24 March 2016
Accepted 13 May 2016
Available online 30 May 2016
Editor: B. Buffett

Keywords:
sea level
eclipse
Common Era ice mass flux
clock error
Earth rotation

ABSTRACT

We predict the perturbation to the Earth's length-of-day (LOD) over the Common Era using a recently derived estimate of global sea-level change for this time period. We use this estimate to derive a time series of "clock error", defined as the difference in timing of two clocks, one based on a theoretically invariant time scale (terrestrial time) and one fixed to Earth rotation (universal time), and compare this time series to millennial scale variability in clock error inferred from ancient eclipse records. Under the assumption that global sea-level change over the Common Era is driven by ice mass flux alone, we find that this flux can reconcile a significant fraction of the discrepancies between clock error computed assuming constant slowing of Earth's rotation and that inferred from eclipse records since 700 CE. In contrast, ice mass flux cannot reconcile the temporal variability prior to 700 CE.

© 2016 Elsevier B.V. All rights reserved.

1. Introduction

Ancient eclipse observations compiled from Babylonian, Chinese, European, and Arab sources provide the primary constraint on changes in the Earth's rotation rate over the past 3000 yr of Earth history (Stephenson and Morrison, 1984, 1995; Stephenson, 1997, 2003). Analyses of these records have yielded a relatively continuous time series since ∼−700 CE of the clock error (ΔT; Fig. 1A), defined as the difference in the timing of an eclipse as measured using timescales that are theoretically-invariant (terrestrial time, TT) or fixed to Earth rotation (universal time, UT). A cubic spline fit through the time series (Stephenson and Morrison, 1995; Stephenson, 1997, 2003) indicates that the clock error accumulates to ∼18000 s, or 5 hr, by −500 CE (Fig. 1A, black line). The first derivative of this spline fit yields the change in the rotation period, or length-of-day (LOD; Fig. 1B, black line). Note that the fit to ΔT in Fig. 1A is constrained to reach a minimum at 1820 CE, when LOD in the TT timescale is precisely 86400 s, and thus changes in the LOD are estimated relative to this date (the black line in Fig. 1B is zero at 1820 CE). All numerical calculations described below will be referenced to the same date.

The clock error monotonically increases as one moves back in time from ∼1820 CE, reflecting a shorter rotation period, or LOD, relative to the value over the past few centuries (Fig. 1B). Stephenson and Morrison (1995) and Stephenson (1997, 2003) characterized the clock error as the combination of a quadratic background trend (Fig. 1A, green line) and a millennial timescale oscillation of ∼1000 s around this trend (green line in Fig. 2A). In this case, the change in the LOD comprises a linear background trend of ∼1.7 ms/century (cy) (∼40 ms since −500 CE; green line, Fig. 1B) and a millennial timescale oscillation with peak-to-peak amplitude of 10 ms (green line in Fig. 2B).

Tidal dissipation produces a significant slowing of the Earth's rotation over time (Lambeck, 2005). Modern satellite geodetic and lunar laser-ranging measurements imply a rate of change of LOD due to this dissipation mechanism of 2.3 ms/cy (Christodoulidis et al., 1988; Williams and Dickey, 2003). If one assumes that the dissipation rate has remained constant since −500 CE, then the red lines in Figs. 1A–B show the clock error and the change in LOD associated with tidal dissipation over this period, respectively. This quadratic signal in Fig. 1A (red line) is often termed the "tidal parabola".

The differences between the time series of the clock error and LOD estimated from the ancient eclipse record and the associated signals due to tidal dissipation are shown in Fig. 2 (red lines). The secular trends in these curves (or the black minus red lines in Figs. 1A, B) are characterized by a clock error

* Corresponding author at: Department of Earth and Planetary Sciences, Harvard University, 20 Oxford Street, Cambridge, MA, 02138, USA.
E-mail address: carlinghay@fas.harvard.edu (C. Hay).

http://dx.doi.org/10.1016/j.epsl.2016.05.020
0012-821X/© 2016 Elsevier B.V. All rights reserved.

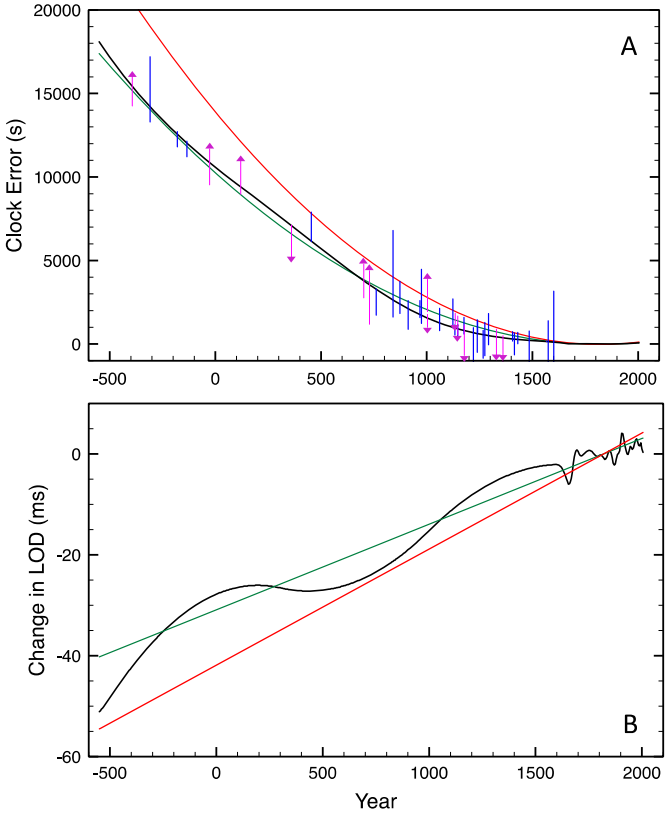

Fig. 1. Changes in Earth rotation over the last 2500 yr inferred from ancient eclipse records. (A) Constraints on clock error from untimed total and annular solar eclipses (blue lines) and untimed partial solar eclipses (magenta, with arrows, showing the start and direction of the allowable bounds) tabulated in Appendix B of Stephenson (1997) (see also Stephenson and Morrison, 1995). Black line – cubic spline fit to the eclipse record, as estimated in Stephenson (1997). Green line – best fitting quadratic form through the same time series, as estimated in Stephenson (1997) ($\Delta T = 31t^2 - 20$ s, where t is measured in centuries from 1820 CE). Red line – clock error associated with the slowing of Earth rotation due to tidal dissipation computed by assuming the dissipation rate is constant and equal to the present rate ($\Delta T = 44t^2 - 20$ s). (B) Black line – change in LOD estimated by (Morrison and Stephenson, 2001) from the associated spline fit in frame (A) and, for the period after ~1600 CE, astronomical observations. Green, red lines – change in LOD associated with the quadratic fit and the tidal parabola, respectively, in frame (A). (For interpretation of the references to color in this figure legend, the reader is referred to the web version of this article.)

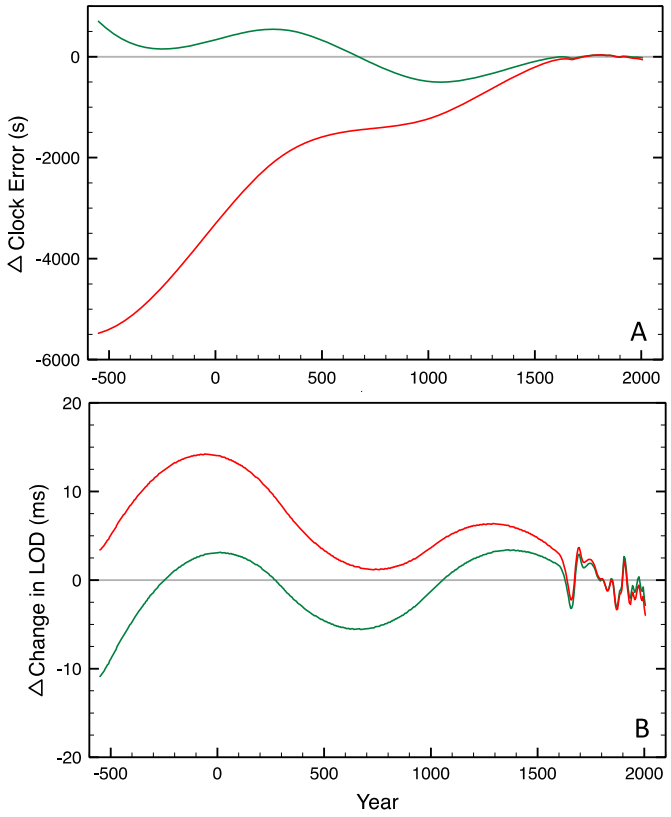

Fig. 2. Discrepancy in Earth rotation over the last 2500 yr relative to a best-fit quadratic curve through the ancient eclipse record. (A) Green line – difference between the cubic spline and quadratic fit to the eclipse-inferred clock error, ΔT, shown in Fig. 1A. Red line – difference between the cubic spline fit to the total clock error, ΔT, and the tidal parabola in Fig. 1A. (B) Green line – difference between the LOD change computed from the spline and quadratic fits in Fig. 1A. Red line – difference between the LOD change computed from the spline fit and the tidal parabola in Fig. 1A. (For interpretation of the references to color in this figure legend, the reader is referred to the web version of this article.)

that grows to ~5400 s, or ~1.5 hr, at −500 CE and a change in LOD of ~0.6 ms/cy. These reflect a non-tidal acceleration of the Earth's rate of rotation, and they have been widely associated with a poleward shift of mass from ongoing glacial isostatic adjustment (GIA) in consequence of the last deglaciation phase of the ice age, which ended ~5 ka (Stephenson and Morrison, 1984, 1995; Stephenson, 1997, 2003; Sabadini et al., 1982; Wu and Peltier, 1984; Vermeersen et al., 1997; Mitrovica et al., 2006), or a combination of GIA and angular momentum exchange between flows in the Earth's outer core and rocky mantle (i.e., core–mantle coupling) (Mitrovica et al., 2015).

The origin of the millennial time scale oscillations in the time series (Fig. 2, green lines), remains enigmatic, and serves as the sole focus of the present study. There have been arguments that these oscillations arise either from core–mantle coupling (Stephenson, 2003; Dumberry and Bloxham, 2006) and/or ice volume changes affecting global sea level (Stephenson, 2003). However, the inferred departure of the clock error from a simple quadratic form is driven by a relatively small set of untimed solar eclipse observations (Stephenson, 1997) (Fig. 3), each of which is subject to a suite of error sources (Stephenson, 1997; Steele and Ptolemy, 2005). (The term "untimed" refers to eclipse observations in which the occurrence of an eclipse was recorded but not the duration; in such cases, timing of the event may be bounded by knowledge of the location of the observation and the nature of the solar eclipse, i.e., total, annular, or partial (Stephenson, 1997).)

Fig. 3 shows the constraint on clock error implied by these observations relative to the best fitting quadratic form. The eleven records have dates of −708 CE, −180 CE, −135 CE, 454 CE, 761 CE, 1133 CE, 1147 CE, 1178 CE, 1221 CE, 1267 CE, and 1361 CE, and the individual constraints imply a minimum departure from the best-fit quadratic of +439 s, 0 s, 0 s, +365 s, −167 s, −293 s, −194 s, −118 s, −112 s, −108 s, and −133 s, respectively (Stephenson, 1997). The consistency in the seven observations spanning the period 761–1361 CE in Fig. 3 suggests that a departure of the clock error from the best-fit quadratic over this period is relatively robust. However, it is clear that the spline fit adopted in Stephenson and Morrison (1995); Stephenson (1997, 2003) (Figs. 1A and 3) may be overestimating the maximum discrepancy of the clock error from a quadratic form within this time interval. The departure from the quadratic form of the observations at both −708 CE and 454 CE is of opposite sign, and it drives the trends in the spline fit for the periods prior to −250 CE and from 0–500 CE, respectively (Fig. 3). In this case, the spline fit may be overestimating the peak amplitude of the millennial scale oscillation prior to 500 CE. For these reasons, we focus in the analysis below on the individual constraints shown in Fig. 3 rather than the

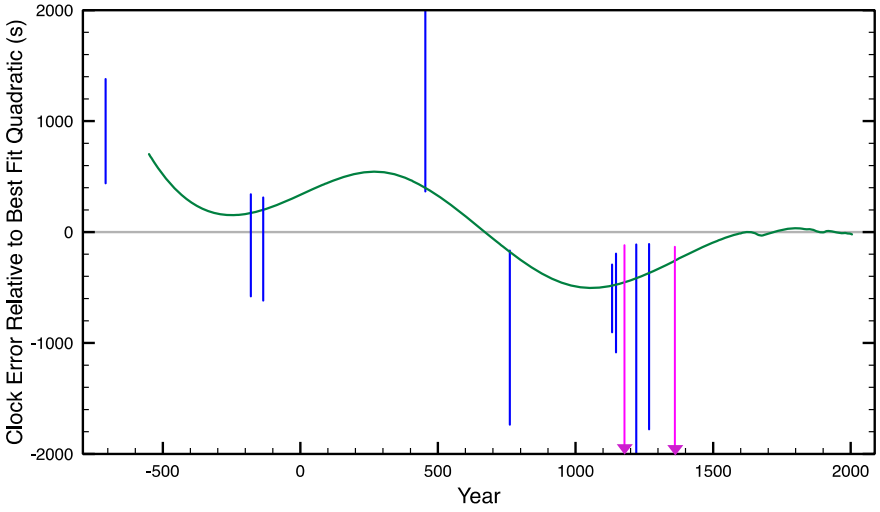

Fig. 3. Clock error relative to the best-fitting quadratic through the full eclipse data set. Clock error, as inferred from a selection of 9 untimed total and annular solar eclipse records (blue lines) and 2 untimed partial solar eclipse records (magenta lines, with arrows) in Fig. 1A (see Fig. 1A caption for description of arrows), relative to the best-fitting quadratic curve through the full eclipse record (i.e., relative to the green line, Fig. 1A). Green line – reproduced from Fig. 2A – difference between the cubic spline and quadratic fit to the eclipse-inferred clock error, ΔT, shown in Fig. 1A. The 11 eclipse records have dates of: −708 CE, −180 CE, −135 CE, 454 CE, 761 CE, 1133 CE, 1147 CE, 1178 CE, 1221 CE, 1267 CE, and 1361 CE. These eclipses were highlighted in Stephenson (1997) as driving the departure of the clock error from a simple quadratic form and, as a consequence, motivating the adoption of the spline fit. Note that the eclipse at −708 CE is off the scale of Fig. 1A. (For interpretation of the references to color in this figure legend, the reader is referred to the web version of this article.)

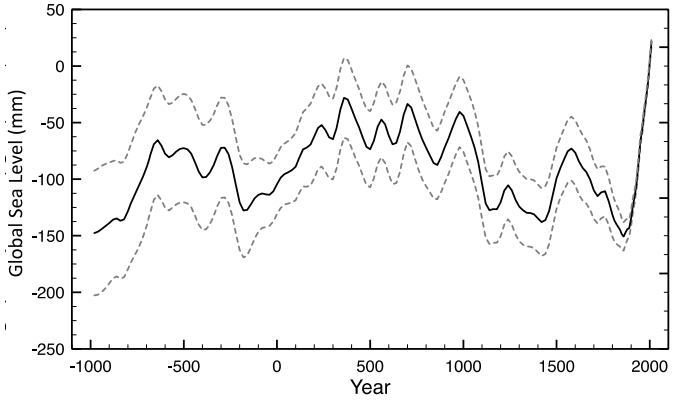

Fig. 4. Global sea level over the last 3000 yr. Global sea level since −1000 CE estimated by Kopp et al. (2016) from a statistical meta-analysis of proxy relative sea-level reconstructions and tide gauge data. The time series was linearly detrended by constraining the global sea-level rate to be zero between 0–1700 CE[16] (see text). Dashed grey lines represent two-sigma uncertainties.

millennial time scale signature inferred from the spline fit through these observations.

During the last decade, high-resolution records of local sea-level changes over the last 3 kyr have become available, Kemp et al. (2011) and these have recently been analyzed within a statistical framework (Kopp et al., 2016) to isolate signals associated with ongoing GIA, global sea-level changes, and regional dynamic effects (e.g., ocean circulation changes). The global sea-level changes, which include contributions from ice mass fluctuations and ocean thermal expansion, show an oscillation in sea level of amplitude ∼0.1 m with several major peaks in the interval 400–1000 CE and minima at (for example) approximately −200 CE, 1100 CE, and 1400 CE (Fig. 4). The curve is also characterized by an exceptionally rapid sea-level rise commencing in the late 19th century (Fig. 4). This bound on the global sea-level variation is consistent, in terms of amplitude, with an earlier published bound based on a less extensive data set (Lambeck et al., 2014) and with a high-resolution sea-level curve from the equatorial Pacific (Woodroffe et al., 2012). Moreover, the global sea-level fall after ∼1000 CE correlates with a ∼0.2 C decline in global mean temperature seen over the same

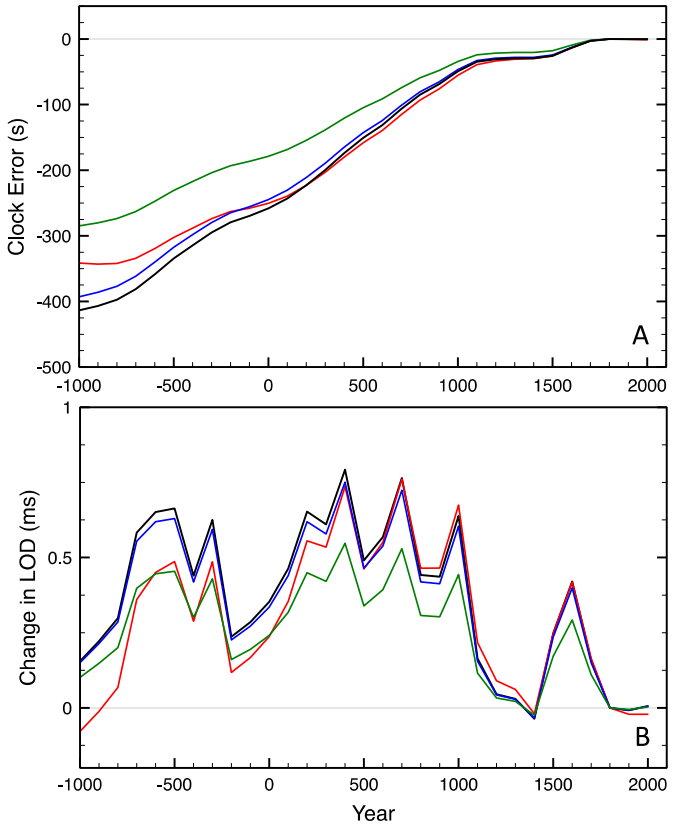

Fig. 5. Numerical predictions of perturbations in Earth rotation due to ice mass changes over the last 3000 yr. Predictions of (A) clock error and (B) changes in LOD driven by ice mass flux with the equivalent global sea-level change shown in Fig. 4. Black lines – predictions generated by adopting the global sea-level change in Fig. 4 and assuming ice mass flux from the WAIS. Blue, green lines – same as the solid black lines, except that the predictions are generated assuming that the global sea-level variation in Fig. 4 is sourced from either the Greenland Ice Sheet or Alaskan glaciers. Red lines – same as the solid black lines, except that the predictions are generated using an Earth model with a lower mantle viscosity of 10^{23} Pa s. (For interpretation of the references to color in this figure legend, the reader is referred to the web version of this article.)

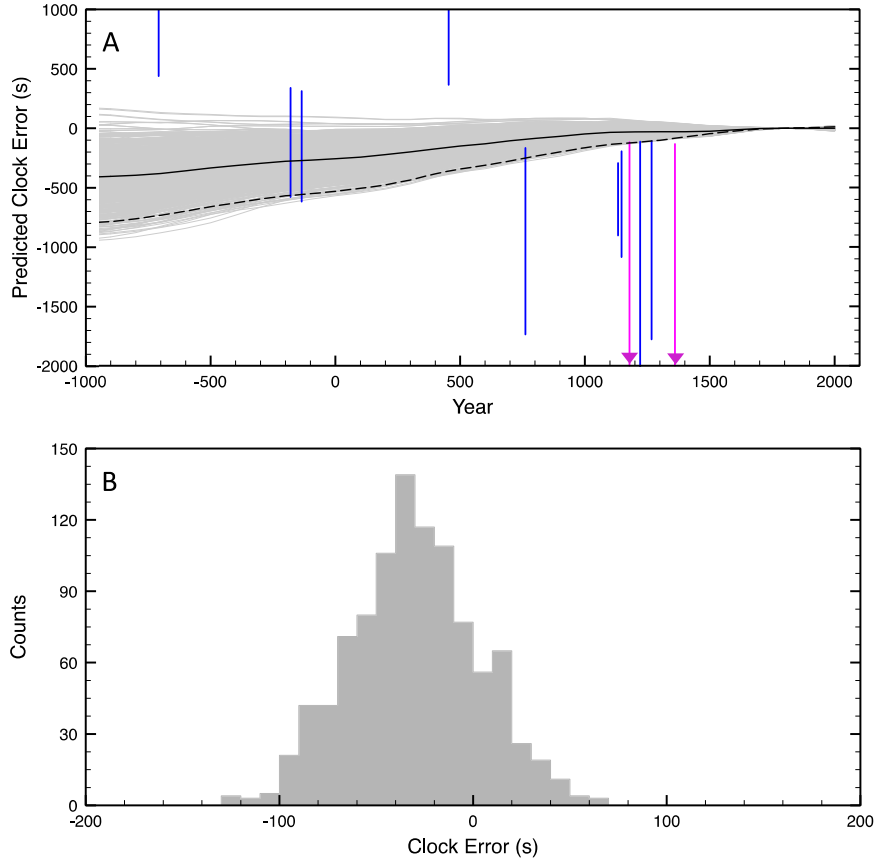

Fig. 6. Monte Carlo simulation of the clock error associated with ice mass flux over the last 3 millennia compared with selected eclipse records. (A) Blue and magenta lines, the latter with arrows identifying the constraints as upper bounds, reproduced from Fig. 3. Grey, shaded lines are predictions of the clock error due to ice mass flux variations constructed from 1000 random samples of the global sea-level time series shown in Fig. 4, where these samples are generated using the full covariance matrix of the probabilistically estimated time series. The 1000 samples are divided into samples that are sourced to the WAIS or the GIS. The black solid line is reproduced from the black line in Fig. 5a. The dashed black line shows the simulation (out of the 1000) that fits the greatest number of eclipse constraints on the figure (see text). (B) Histogram of the 1000 predictions of clock error at 1200 CE. (For interpretation of the references to color in this figure legend, the reader is referred to the web version of this article.)

period (Marcott et al., 2013). We note that typical rates of long-term sea-level rise on Fig. 4 (e.g., from −180 CE to 360 CE) are ∼0.2 mm/yr, nearly an order of magnitude smaller than the rate over the past few decades (Church et al., 2013) (see also Kopp et al., 2016).

2. Discussion

2.1. Clock error driven by sea-level changes

To assess the extent to which ice-mass changes may have contributed to the signal in Fig. 3, we computed perturbations in Earth rotation based upon the sea-level history in Fig. 4 and performed a series of sensitivity tests. In these numerical predictions, we assume that all of the sea-level variability is sourced entirely from either the Greenland Ice Sheet (GIS), the West Antarctic Ice Sheet (WAIS), or (as an example of a mountain glacier system) Alaskan glaciers. Warming raises sea level through expansion of ocean water, which does not affect Earth rotation significantly, and thus by sourcing all sea-level changes from ice, our predictions represent upper bounds. Our numerical tests also explore the sensitivity of the predictions to variations in Earth structure, and they include a Monte-Carlo analysis in which we consider a large number of ice mass histories consistent with the probabilistic bounds summarized in Fig. 4.

Our calculations require, on input, models for the history of ice cover and depth-varying viscoelastic Earth structure. Using these models, we compute gravitationally self-consistent sea-level variations using a theory (Kendall et al., 2005) that accounts for migrations of shorelines, changes in the extent of marine-based ice, and the feedback into sea level of perturbations in the magnitude and orientation of the rotation vector. The latter are computed using the rotational stability theory described in Mitrovica et al. (2005). The calculations yield predictions for a variety of observables, including a time series of changes to the Earth's rotation period, or LOD. This time series is then used to compute a time series for the clock error via a backward integration referenced to an origin at 1820 CE. All calculations described below adopt elastic and density profiles given by the seismic model PREM (Dziewonski and Anderson, 1981).

To begin, we adopt the ICE5G model for the ice geometry across the last glacial cycle, and the VM2 viscosity profile to which the ICE5G model is paired (Peltier, 2003). We then run additional calculations in which the ICE5G history is augmented to include changes in polar ice volume over the last 3 ka that match the global sea-level changes shown in Fig. 4 (with the exception that we do not include the rapid sea-level rise across the 20th century). Taking the difference between the output from each of these runs and the standard ICE5G/VM2 run yields a perturbation in the clock error and changes in LOD associated with recent ice mass changes (Fig. 5).

Fig. 5 (black lines) shows the results of a calculation in which the global sea-level change (and associated ice mass flux) is sourced entirely to the West Antarctic Ice Sheet (WAIS). The pre-

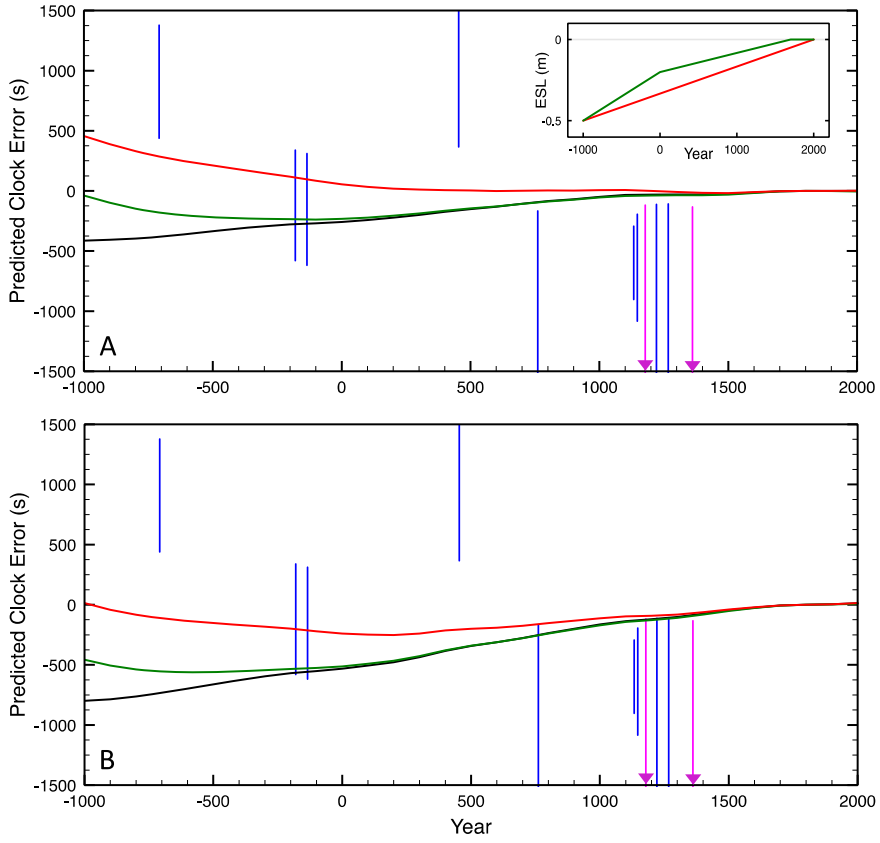

Fig. 7. Numerical predictions of clock error associated with ice mass flux over the last 3 millennia. (A) Solid black line is reproduced from Figs. 5A and 6A. Green and red lines are predictions of clock error based on a calculation in which the global sea level used to compute the black line is augmented to add the (similarly colored) background eustatic sea-level (ESL) trend shown in the inset (see text). (B) Same as (A), except the black line is the same as the dashed black line in Fig. 6A. Eclipse data set is reproduced from Fig. 3. Inset – Background global sea-level curves (adapted from Woodroffe et al. (2012)) that are added to the statistically derived sea-level histories used to compute the solid black line on each frame. (For interpretation of the references to color in this figure legend, the reader is referred to the web version of this article.)

dicted change in the LOD (Fig. 5B) shows a decrease in the LOD of ∼0.8 ms from 700 CE to 1400 CE. This trend is as expected from Fig. 4, since a growth in polar ice (equivalent to a eustatic sea-level fall of ∼0.1 m) over this time window will bring mass from the low latitudes to high latitudes and increase the rotation rate. The predicted clock error increases from approximately −30 s at 1200 CE to −150 s at 500 CE and to −260 s by 0 CE (Fig. 5A). The first of these values is a factor of ∼3–5 smaller than the departure of the clock error from a best-fit quadratic form inferred from untimed solar eclipses with ages 1133–1361 CE (Fig. 6A). The predicted clock error at 500 CE (−150 s) is approximately half the amplitude of the departure from quadratic implied by the solar eclipse recorded at 454 CE, but it is of opposite sign (Fig. 6A).

Fig. 5 also shows predictions that source the global sea-level variation in Fig. 4 to either the Greenland Ice Sheet (blue lines) or Alaskan glaciers (green lines), or to the WAIS but adopting a different model of the radial viscosity structure of the Earth's mantle (red lines). The VM2 model is characterized by a viscosity that varies from 1×10^{21} Pa s at the top of the lower mantle to $\sim 3 \times 10^{21}$ Pa s near the core mantle boundary; the alternate Earth model considered in Fig. 5 has a significantly higher viscosity of 10^{23} Pa s in this region (see, for example, Vermeersen et al., 1997).

The calculations are relatively insensitive to the adopted viscosity model. This insensitivity reflects the relatively short time scale of the surface mass loading implied by Fig. 4, and in this case elastic effects dominate the deformation driven by the loading. Therefore, for a given ice flux geometry, the change in the LOD due to ice mass variations over the past 3 kyr will be approximately proportional to the total change in global sea level.

Predictions of perturbations in the rotation rate are sensitive only to the long wavelength (spherical harmonic degree two) spatial geometry of the loading and are insensitive to whether this loading occurs in the northern or southern hemisphere (Mitrovica and Peltier, 1993). As a consequence, choosing either of the two polar ice sheets as the source for the global sea-level change has little impact on these predictions. In contrast, sourcing the sea-level change to lower latitude Alaskan glaciers reduces the predicted clock error and change in LOD by ∼30% relative to predictions that adopt a GIS or WAIS source.

2.2. Monte Carlo tests

In the next sensitivity test, we generated 1000 samples from the sea-level probability distribution summarized in Fig. 4 and repeated our numerical analysis for each time series. The simulations were divided between cases in which the global sea-level change was sourced to the GIS or WAIS. We superimpose, in Fig. 6A, the predicted clock error associated with each of the 1000 simulations onto the eleven eclipse-inferred departures from the best-fit quadratic form originally shown in Fig. 3. A histogram of the predictions at 1200 CE is provided in Fig. 6B. The solid black line in Fig. 6A is reproduced from Fig. 5A. The dashed black line is the clock error for the simulation (out of the total of 1000) that is consistent with the greatest number of eclipse constraints. This line intersects 6 of these constraints.

A more general search for the best-fit time series of clock error would also allow for a variation in the quadratic signal. To explore this possibility, we also performed a test in which we added a wide range of quadratic signals (with magnitudes up to ∼5000 s at

−1000 CE) to the clock error computed for each of the 1000 simulations and counted the number of eclipse constraints that were fit by each time series. In this exercise, we rejected any simulation that misfit the eclipse record at −180 CE in order to exclude time series that fit the youngest seven eclipse records in Fig. 6A (by adding a quadratic with very large negative values of clock error to the original 1000 simulations) but that were characterized by huge (>1000 s) misfits to the four oldest eclipse constraints. We found that no more than 6 eclipse records were fit, and in each of these best-fit cases the total clock error showed only minor differences with the dashed black line in Fig. 6A.

As noted above, the seven youngest eclipse records in Fig. 6A, with dates of 761 CE, 1133 CE, 1147 CE, 1178 CE, 1221 CE, 1267 CE, and 1361 CE, suggest minimum departures of the clock error from a best-fit quadratic of −167 s, −293 s, −194 s, −118 s, −112 s, −108 s, and −133 s, respectively. At these specific ages, the clock errors predicted from the simulation shown by the black dashed line in the Fig. 6A are −252 s, −131 s, −129 s, −124 s, −117 s, −108 s, and −85 s, respectively (Fig. 6A). We thus conclude that ice mass flux changes may have been responsible for a significant fraction of the departure of the eclipse-inferred clock error from a best-fit quadratic during the past 1300 yr. To explore this issue further, consider the histogram in Fig. 6B. While only 1% of the simulations predict a clock error of magnitude comparable to that inferred from the eclipse records at ∼1200 CE (i.e., ∼110 s), ∼25% of the simulations predict a clock error exceeding 50% of this magnitude.

A more definitive conclusion regarding the contribution of ice mass flux to the clock error in this period, and the necessity of invoking other processes such as momentum exchange between the Earth's core and mantle (Dumberry and Bloxham, 2006), or variability in tidal dissipation, will require that uncertainties in the global sea-level history (Fig. 4), and the associated distribution of sources (including the signal from thermal expansion), be reduced. In regard to the latter, and as discussed in the context of Fig. 5, if glaciers dominated any ice sheet contributions to the sea-level history, then the clock errors predicted in Fig. 6 would be reduced.

Two of the four oldest eclipse observations in Fig. 6A, at −180 CE and −135 CE, are consistent with the range of predictions associated with ice mass fluctuations. (They are also consistent with the best-fit quadratic and cubic spline time series of clock error.) The remaining two eclipses, at −708 CE and 454 CE, are characterized by minimum clock errors of +439 s and +365 s, respectively, relative to the best-fit quadratic, whereas ice mass fluctuations generated from the probabilistic estimate of sea-level change yield maximum clock errors of 130 s and 80 s at these times (Fig. 6A). It is unlikely that all the eclipse-based inferences of clock error from −708 CE to 761 CE could be simultaneously reconciled by any plausible ice mass flux. As an example, invoking ice mass flux alone to explain the 530 s shift in clock error from 454 CE to 761 CE in Fig. 6A would require an associated global sea-level rise of ∼1 m during the same time interval, a trend clearly ruled out by the geological record (Kopp et al., 2016; Lambeck et al., 2014; Woodroffe et al., 2012) (Fig. 4).

2.3. Alternative sea-level histories

The global sea-level history in Fig. 4 (Kopp et al., 2016) was linearly detrended so that the global sea-level rate between 0–1700 CE was removed, and thus it is possible that a moderate background trend is missing from this probabilistically derived time series. To investigate the potential impact of such a trend, we have repeated the GIA predictions that yielded the solid and dashed black lines in Fig. 6A, but have augmented the global sea-level history adopted in each of these predictions using two

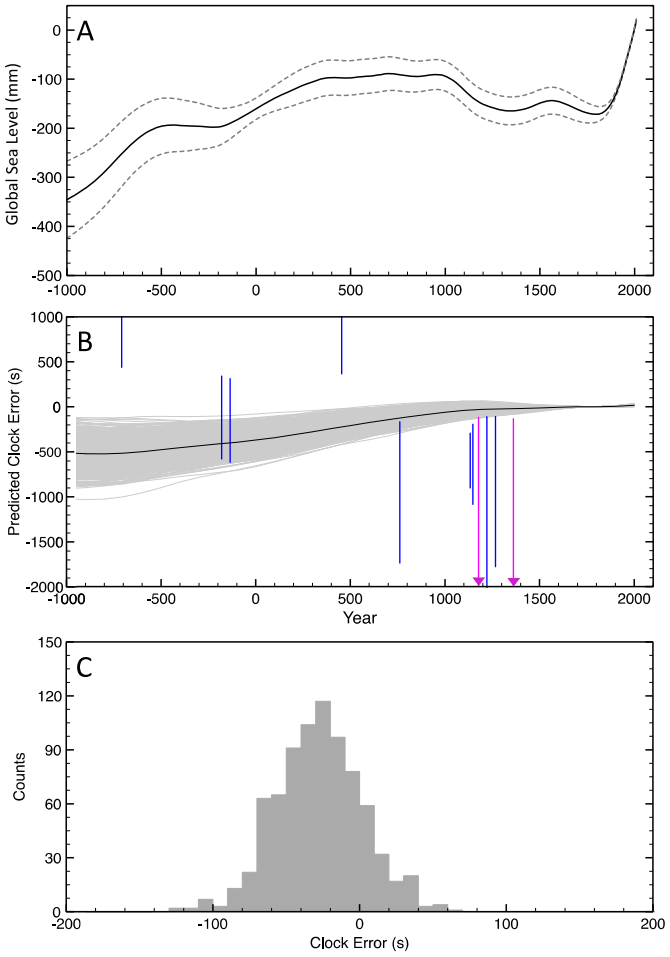

Fig. 8. Analysis of ancient eclipse records based on an alternate time series of global sea-level change over the last three millennia. (A) The global sea-level time series since −1000 CE estimated in Kopp et al. (2016) using the priori $ML_{2,2}$. Dashed grey lines represent two-sigma uncertainties. (B, C) Analogous to Figs. 6A and 6B, respectively, except that the simulations are based on the probabilistic assessment of global sea-level change shown in (A). The solid black line in (B) is the clock error computed using the global sea-level time series given by the solid line in (A). (For interpretation of the references to color in this figure legend, the reader is referred to the web version of this article.)

different background eustatic trends, both adapted from Woodroffe et al. (2012). The first of these trends follows the eustatic curve inferred in Woodroffe et al. (2012) and it is characterized by a 0.3 m rise in global sea level from −1000 CE to 0 CE, a 0.2 m increase from 0–1700 CE, and no change from 1700 CE to the present (Fig. 7 inset, green line). The second background trend assumes a constant rate of rise, yielding a 0.5 m increase in global sea level from −1000 CE to the present (Fig. 7 inset, red line). The results of these additional calculations are shown in Fig. 7.

The incorporation of a background trend in ice melting acts to slow the rotation rate and to bring the predicted clock errors higher (i.e., toward more positive values), particularly prior to 1000 CE. In the case of the multi-stage background trend (Fig. 7 inset, green line), the level of fit to the eclipse record is essentially unchanged. Incorporating the uniform melt trend (Fig. 7 inset, red line) into the model sea-level history has a more significant impact on the predicted clock error; this impact has an approximately quadratic form. In the simulation of Fig. 7A (red line), this leads to a reduced misfit to the eclipse records at −708 CE and 454 CE, but increased misfit to more recent eclipse records. While the improved fit to the eclipse record at −708 CE is intriguing, our conclusion that ice mass flux cannot simultaneously reconcile all

eclipse-based inferences of clock error from −708 CE to 761 CE is unchanged.

Finally, Kopp et al. (2016) considered the sensitivity of their estimate of global sea-level change across the past three millennia (Fig. 4) to the prior model adopted in the Bayesian analysis. To investigate whether this sensitivity has implications for our analysis, we repeated the calculations in Fig. 6 using the global sea-level time series derived in Kopp et al. (2016) using the prior $ML_{2,2}$ (see their Fig. S3b). This alternate time series is shown in Fig. 8A and the results of our clock error analysis based upon it are summarized in Figs. 8B and 8C. Once again, while these predictions suggest that ice mass flux may have contributed significantly to the clock error estimated from the eclipse record of the past 1300 yr, this flux cannot fully capture the variability in clock error evident in the eclipse record prior to 761 CE. Thus, if all these earlier eclipse records are accurate, then processes other than ice mass changes likely dominate the millennial scale trends in clock error across this time interval.

Acknowledgements

The authors would like to thank Roberto Sabadini and one anonymous reviewer for their helpful comments and feedback. This work was supported by the U.S. National Science Foundation (grants ARC-1203415 to REK and CH; ARC-1203414 to JXM; 1338832 and 0424589 to RBA; AGS-1304309 to PH).

References

Christodoulidis, D.C., Smith, D.E., Williamson, R.G., Klosko, S.M., 1988. Observed tidal braking in the Earth/Moon/Sun system. J. Geophys. Res. 93, 6216–6236.

Church, J.A., et al., 2013. Sea level change. In: Stocker, T.F., et al. (Eds.), Climate Change 2013: The Physical Science Basis. Contribution of Working Group I to the Fifth Assessment Report of the Intergovernmental Panel on Climate Change. Cambridge University Press, Cambridge, United Kingdom.

Dumberry, M., Bloxham, J., 2006. Azimuthal flows in the Earth's core and changes in length of day at millennial timescales. Geophys. J. Int. 165, 32–46.

Dziewonski, A.M., Anderson, D.L., 1981. Preliminary reference Earth model. Phys. Earth Planet. Inter. 25, 297–356.

Kemp, A.C., Horton, B.P., Donnelly, J.P., Mann, M.E., Vermeer, M., Rahmstorf, S., 2011. Climate related sea-level variations over the past two millennia. Proc. Natl. Acad. Sci. 108, 11017–11022.

Kendall, R., Mitrovica, J.X., Milne, G.A., Tamisiea, M.E., 2005. On post-glacial sea level – II. Numerical formulation and comparative results on spherically symmetric models. Geophys. J. Int. 161, 679–706.

Kopp, R.E., Kemp, A.C., Bittermann, K., Horton, B.P., Donnelly, J.P., Gehrels, W.R., Hay, C.C., Mitrovica, J.X., Morrow, E.D., Rahmstorf, S., 2016. Temperature-driven global sea-level variability in the Common Era. Proc. Natl. Acad. Sci. 113 (11), E1434–E1441.

Lambeck, K., 2005. The Earth's Variable Rotation: Geophysical Causes and Consequences. Cambridge Univ. Press, p. 464.

Lambeck, K., Rouby, H., Purcell, A., Sun, Y., Sambridge, M., 2014. Sea level and global ice volumes from the Last Glacial Maximum to the Holocene. Proc. Natl. Acad. Sci. 111, 15296–15303.

Marcott, S.A., Shakun, J.D., Clark, P.U., Mix, A.C., 2013. A reconstruction of regional and global temperature for the past 11,300 years. Science 339, 1198–1201.

Mitrovica, J.X., Peltier, W.R., 1993. Present-day secular variations in the zonal harmonics of the Earth's geopotential. J. Geophys. Res. 98, 4509–4526.

Mitrovica, J.X., Wahr, J., Matsuyama, I., Paulson, A., 2005. The rotational stability of an ice age Earth. Geophys. J. Int. 61, 491–506.

Mitrovica, J.X., Wahr, J., Matsuyama, I., Paulson, A., Tamisiea, M.E., 2006. Reanalysis of ancient eclipse, astronomic and geodetic data: a possible route to resolving the enigma of global sea-level rise. Earth Planet. Sci. 243, 390–399.

Mitrovica, J.X., Hay, C.C., Morrow, E., Kopp, R.E., Dumberry, M., Stanley, S., 2015. Reconciling past changes in Earth rotation with 20th century global sea-level rise: resolving Munk's enigma. Sci. Adv. 1 (11), e1500679.

Morrison, L.V., Stephenson, F.R., 2001. Historical eclipses and the variability of the Earth's rotation. J. Geodyn. 32, 247–265.

Peltier, W.R., 2003. Global glacial isostasy and the surface of the ice-age Earth: the ICE-5G (VM2) model and GRACE. Annu. Rev. Earth Planet. Sci. 32, 111–149.

Sabadini, R., Yuen, D.A., Boschi, E., 1982. Polar wandering and the forced responses of a rotating, multilayered, viscoelastic planet. J. Geophys. Res. 87, 2885–2903.

Steele, Ptolemy, J., 2005. Babylon and the rotation of the Earth. Astron. Geophys. 46, 5.11–5.15.

Stephenson, F.R., 1997. Historical Eclipses and Earth's Rotation. Cambridge Univ. Press, p. 464.

Stephenson, F.R., 2003. Historical eclipses and Earth's rotation. Astron. Geophys. 44, 2.22–2.27.

Stephenson, F.R., Morrison, L.V., 1984. Long-term changes in the rotation of the Earth: 700 B.C. to A.D. 1980. Philos. Trans. R. Soc. Lon. 313, 47–70.

Stephenson, F.R., Morrison, L.V., 1995. Long-term fluctuations in the Earth's rotation: 700 BC to AD 1990. Philos. Trans. Phys. Sci. Eng. 351, 165–202.

Vermeersen, L.L.A., Fournier, A., Sabadini, R., 1997. Changes in rotation induced by Pleistocene ice masses with stratified analytical Earth models. J. Geophys. Res. 102, 27689–27702.

Williams, J.G., Dickey, J.O., 2003. Lunar geophysics, geodesy, and dynamics. In: Noomen, R., Klosko, S.M., Noll, C., Pearlman, M. (Eds.), 13th International Workshop on Laser Ranging. Washington, D.C., pp. 75–86.

Woodroffe, C.D., McGregor, H.V., Lambeck, K., Smithers, S.G., Fink, D., 2012. Mid-Pacific microatolls record sea-level stability over the past 5000 yr. Geology 40, 951–954.

Wu, P., Peltier, W.R., 1984. Pleistocene deglaciation and the Earth's rotation: a new analysis. Geophys. J. R. Astron. Soc. 76, 753–791.